Influence of mini warm pool extent on phytoplankton productivity and export in the Arabian sea

Nicholas Bock, Joaquim Goes, Hervé Claustre, Vincent Taillandier, Helga Do Rosario Gomes

Deep–Sea Research I 214 (2024) 104406

Contents lists available at ScienceDirect

Deep-Sea Research Part I

journal homepage: www.elsevier.com/locate/dsri

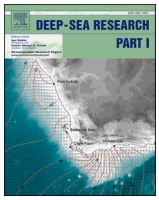

Influence of mini warm pool extent on phytoplankton productivity and export in the Arabian sea

Nicholas Bock [a,b,*], Joaquim Goes [b], Hervé Claustre [a], Vincent Taillandier [a], Helga do Rosario Gomes [b]

[a] CNRS & Sorbonne Université, Laboratoire d'Océanographie de Villefranche, LOV, Villefranche-sur-Mer, France
[b] Lamont-Doherty Earth Observatory, Columbia University, Palisades, NY, USA

ARTICLE INFO

Keywords:
Arabian sea
BGC-Argo
Phytoplankton production
Climate change

ABSTRACT

The Arabian Sea is a highly productive tropical ecosystem of the Indian Ocean that supports high fluxes of particulate organic carbon to the mesopelagic zone from two distinct periods of elevated biological productivity associated with the semiannual reversals of the monsoonal wind system. There are now strong indications that the Arabian Sea's monsoonal wind patterns and hydrographic conditions are being impacted by long-term temperature increases, but the consequences of these changes on primary production and carbon export to the mesopelagic zone are unknown. This is especially true for the summer monsoon period when cloud cover obscures much of the Arabian Sea basin and therefore precludes remotely sensed ocean color measurements for estimating phytoplankton biomass and productivity. Here we overcome this limitation by using a database of bio-optical profiles from Biogeochemical Argo floats collected over the last decade to evaluate the impact of interannual temperature increases on Arabian Sea primary production and carbon export. We classify individual years of float observations based on the spatial extent of the Arabian Sea Mini Warm Pool that appears in the southeast Arabian Sea before the onset of the summer monsoon. This Mini Warm Pool, which begins to build in winter and collapses with the onset of the summer monsoon in late spring, has gained considerable interest on account of its influence on the timing of the onset of the summer monsoon. We observed a 35 percent decrease in primary production during the summer monsoon phytoplankton bloom in strong warm pool years, and a 13 percent decrease in particle stocks in the upper mesopelagic zone following the peak of the bloom. Decreases in production and export were additionally accompanied by a decrease in average particle size, indicating a shift from larger cells like diatoms that appear from fertilization of the oligotrophic waters to smaller phytoplankton size classes in response to a deepening of the thermocline and increased stratification of the water column. These results suggest changes in phytoplankton community structure and further decreases in primary production and carbon export in the Arabian Sea in response to future warming.

1. Introduction

The Arabian Sea is one of the most biologically productive regions of the ocean, supporting global maximal fluxes of particulate organic carbon (POC) to the mesopelagic zone (Nair et al., 1989; Haake et al., 1993; Goes et al., 2005; Honjo et al., 2008). Phytoplankton primary production and the functioning of the biological carbon pump in the Arabian Sea are strongly influenced by the seasonally reversing winds of the Asian Monsoon and the resulting changes in near-surface hydrology (Nair et al., 1989; Haake et al., 1993; Ramaswamy and Nair, 1994). During June and July, winds propagating from the southwest drive extensive upwelling along the Somali, Yemeni and Omani coasts, delivering nutrient-rich water to the surface that support extensive phytoplankton blooms throughout the western Arabian Sea (Currie et al., 1973; Bauer et al., 1991). During December and January, winds propagating from the Himalayan Mountain Range in the northeast drive surface cooling, resulting in increased vertical mixing (Banse and McClain, 1986). These monsoon periods are punctuated by inter-monsoon periods of reduced wind stress, enhanced warming coupled with strong stratification of surface waters, and the formation of deep chlorophyll maxima following the depletion of surface nutrients.

One of the main features in Arabian Sea hydrology is the annual formation of the Arabian Sea Mini Warm Pool (ASMWP; see Table 1 for a list of abbreviations used in this study), a region of elevated sea surface

* Corresponding author. CNRS & Sorbonne Université, Laboratoire d'Océanographie de Villefranche, LOV, Villefranche-sur-Mer, France.

https://doi.org/10.1016/j.dsr.2024.104406
Received 14 October 2023; Received in revised form 31 July 2024; Accepted 17 October 2024
Available online 24 October 2024

Table 1
Abbreviations usedin this study.

Abbr	Definition	Units
ASMWP	Arabian Sea Mini Warm Pool	
b_{bp}	Backscatter	m^{-1}
BVF_{MLD}	Brunt-Vaisala Frequency at the mixed layer depth	s^{-1}
[Chl*a*]	Chlorophyll *a* concentration	mg m^{-3}
$[Chla]_{EZ}$	Average [Chl*a*] within the euphotic zone	mg m^{-3}
d_{ML}	Average particle diameter within the mixed layer	μm
DMI_{FIM}	Dipole Mode Index during preceding FIM period	m
EZ	Euphotic Zone depth horizon	m
FIM	Fall Intermonsoon	
MLD	Mixed Layer Depth	m^2
MZ_{1-4}	Mesopelagic zone depth horizons 1–4	m
NEM	Northeast Monsoon	
NPP_{EZ}	Net primary production within the euphotic zone	mg C m^{-2} d^{-1}
OMZ	Oxygen Minimum Zone	
SIM	Spring Intermonsoon	
$strI_{\sigma}$	Stratification Index	kg m^{-3}
SWM	Southwest Monsoon	
TCline	Thermocline Depth	m
WIN_{FIM}	Western Indian Ocean SST anomaly during preceding FIM period	°C
WP_{IND}	Average normalized warm pool index	

temperature (SST) off the southwest coast of India that reaches its maximal areal extent during the spring intermonsoon period between April and May and collapses with the onset of the Indian summer monsoon (Rao et al., 2015). The magnitude of the ASMWP has been identified as one of the key factors influencing the timing of the monsoon onset (Rao and Sivakumar, 1999; Deepa et al., 2012) and summer monsoon rainfall over India (Neema et al., 2012). In addition to the maximum solar radiation, the clear sky and weaker winds in spring which give rise to the mini warm pool, intrusion of the low saline waters from the Bay of Bengal during late fall and winter create a vertical barrier layer that is also believed to contribute to the existence of the ASMWP (Masson et al., 2005).

An increase in the ASMWP extent generally leads to a larger area of the southwestern Arabian Sea becoming stratified (Neema et al., 2012), which could limit production by inhibiting water column turbulence and vertical fluxes of nutrients into the euphotic zone during the spring intermonsoon (SIM) and southwest monsoon (SWM) periods. However, it has been challenging to study the impact of the ASMWP extent on phytoplankton productivity and export, in large part because of the limited availability of contemporary in-situ datasets. Additionally the build-up of clouds prior to and following the onset of the SWM limits the ability of ocean color satellites to provide measurements of phytoplankton biomass and productivity from space.

Here to circumvent the limitations imposed by the paucity of shipboard and satellite datasets, we have relied on the Biogeochemical Argo (BGC-Argo; Argo, 2024) network of autonomous profiling floats to understand the role of the ASMWP on phytoplankton productivity and carbon export of which very little is known. This dataset provides a rich time series of hundreds of depth profiles of bio-optical and biogeochemical measurements made over the last ten years in the Arabian Sea, thus allowing new perspectives on interannual variability in ecosystem response to climate forcing.

In this study, we have taken advantage of this vast repository of data from BGC-Argo floats, in combination with data from remote sensing platforms, to evaluate the impact of ASMWP extent on seasonality in primary production and carbon export within open-ocean regions of the Arabian Sea. We have also evaluated the hydrological and biogeochemical drivers of this production and the associated particle dynamics within the mesopelagic zone including the Arabian Sea Oxygen Minimum Zone (OMZ), the thickest OMZ in the global ocean (Rixen et al., 2020). Additionally, we evaluate relationships between the Warm Pool extent and the functioning of the Indian Ocean Dipole (IOD), which can contribute to elevated SST anomalies in the Western Indian Ocean during September–November and may play a role in ASMWP formation. Beyond capturing relationships between phytoplankton ecophysiology and Arabian Sea hydrology, our results highlight the possibility of continued decreases in primary production and carbon in the region in response to future warming.

2. Methods

2.1. Data sources

The study region was defined as the area within 5°N – 26°N and 50°E – 80°E, and excluding the marginal Gulf of Aden and the Sea of Oman. Daily SST measurements for the years 2002–2022 were obtained from the Group for High Resolution Sea Surface Temperature (GHRSST) Multiscale Ultrahigh Resolution (MUR) L4 dataset (NASA/JPL, 2022). Measurements of daily averaged surface photosynthetically active radiation (I_0; mol photon m^{-2} day^{-1}) were obtained from The Suomi National Polar-orbiting Partnership Visible Infrared Imaging Radiometer Suite (SNPP-VIIRS; NASA Ocean Biology Processing Group, 2022). On account of the significant role played by the Indian Ocean Dipole on hydrographic conditions in the Arabian Sea, we obtained Dipole Mode Index data and SST anomalies for the Western Indian Ocean from the National Oceanic and Atmospheric Administration's Global Climate Observing System Working Group on Surface Pressure (https://psl.noaa.gov/gcos_wgsp/Timeseries/DMI/). Measurements of monthly averaged wind stress magnitude (Wind Stress; pa) were obtained from the Meteorological Operational Satellite (METOP) Advanced Scatterometer (ASCAT; NOAA, 2024). Level 4 measurements of sea surface height anomalies (SSHA; m) were obtained from the NASA Making Earth System Data Records for Use in Research Environments (MEaSUREs) project (Fournier et al., 2022). SSHA measurements from pixels near the Omani, Somali, and Western Indian Coasts were classified as belonging to upwelling regions (Supplementary Fig. 1). SSHA measurements from pixels within the overall study area, excluding upwelling regions, were classified as belonging to the Central Basin.

BGC-Argo float data were accessed through the Argo Global Data Assembly Centre (Argo, 2024). Hydrological data (e.g., temperature, practical salinity, and density) collected by SBE 41 Seabird CTD sensors were processed and quality-controlled following Argo protocols as described by Wong et al. (2020). Floats were additionally equipped with 1) Seabird-Wetlabs FLBB sensors including a chlorophyll fluorometer (excitation at 470 nm; emission at 695 nm) and a backscattering sensor at 700 nm, and 2) Aanderaa Oxygen Optodes measuring concentrations of dissolved oxygen. Measurements of Chlorophyll *a* ([Chl*a*] mg m^{-3}), optical backscatter (b_{bp}; m^{-1}), and dissolved oxygen (O_2; μmol kg^{-1}) were quality controlled following BGC-Argo protocols (Thierry et al., 2011; Schmechtig et al., 2015, 2018a, 2018b). Non-photochemical quenching in near-surface measurements of [Chl*a*] was corrected following Xing et al. (2012). Drift in the sensitivity of oxygen optode sensors and differences in sensor gain settings between floats were corrected during delayed-mode processing as described in Thierry et al. (2021).

2.2. Classification of SST time series

Individual dates within the MUR SST dataset were classified as belonging to one of the four periods of the Asian monsoon cycle: Northeast Monsoon (NEM; named for winds propagating from the northeast), Spring Intermonsoon (SIM), Southwest monsoon (SWM; named for winds propagating from the southwest), or Fall Intermonsoon (FIM). For NEM and SWM, classifications were performed by identifying the minimal average daily SST value within December, February, and March (for NEM) or June, July, and August (for SWM). For SIM and FIM, classifications were performed by identifying the maximal average daily SST value within March, April, and May (for SIM) or September,

October, and November (for FIM). The start/end dates of each period were then determined as the dates intermediate to the preceding and subsequent maximum or minimum.

ASMWP extent was evaluated following the method described in Rao et al. (2015). Briefly, the ASMWP index was calculated from daily MUR SST data as the spatial integral of the difference between SST and 30 °C within −10°N – 26°N and 50°E – 80°E. To account for differences in the resolution of satellite images or the degree of cloud cover, ASMWP Index values were then normalized to the total number of measurement-containing pixels within the study area. Normalized ASMWP Index values were then averaged within the SIM period for each year (hereafter WP_{IND}). Finally, the mean and standard deviation of WP_{IND} were calculated for all years in the MUR SST time series (2002–2022). Years with WP_{IND} values within 0.5 standard deviations of the mean were classified as normal warm pool years. Years with WP_{IND} values exceeding greater or less than 0.5 standard deviations of the mean were classified as strong warm pool years or weak warm pool years, respectively. However, because this method only resulted in one weak warm pool year within the date range of the float dataset, our analysis focuses only on contrasts between years from normal and strong warm pool regimes.

2.3. Processing of float data

2.3.1. Construction of float dataset

Only [Chl*a*], b_{bp}, and O_2 measurements with delayed mode quality control flags of 1 (good data) or 2 (probably good data) were included in the analyses. Profiles with average [O_2] of less than 4 μM between 200 and 300 m were defined as being located within the core OMZ, following Wojtasiewicz et al. (2020). Profiles outside of the core OMZ were excluded from analyses. This filtering step provided a final dataset of 1502 individual profiles from 24 floats deployed between the years 2013 and 2022 (Fig. 1; Table 2).

2.3.2. Characterization of water column hydrology and biogeochemistry

Mixed layer depths were calculated as the depth where practical density increased by 0.03 kg m^{-3} relative to the density at a reference depth of 10 m. To characterize stratification in the water column, the stratification index ($strI_\sigma$) was calculated as the difference in potential density between the surface and a depth of 200 m (Behrenfeld et al., 2006). The Brunt Väisälä frequency was additionally calculated at the depth of the MLD (BVF_{MLD}) to characterize stratification at the mixed layer boundary. To calculate the thermocline depth, temperature profiles were interpolated to 1 m resolution. Rolling regressions were then

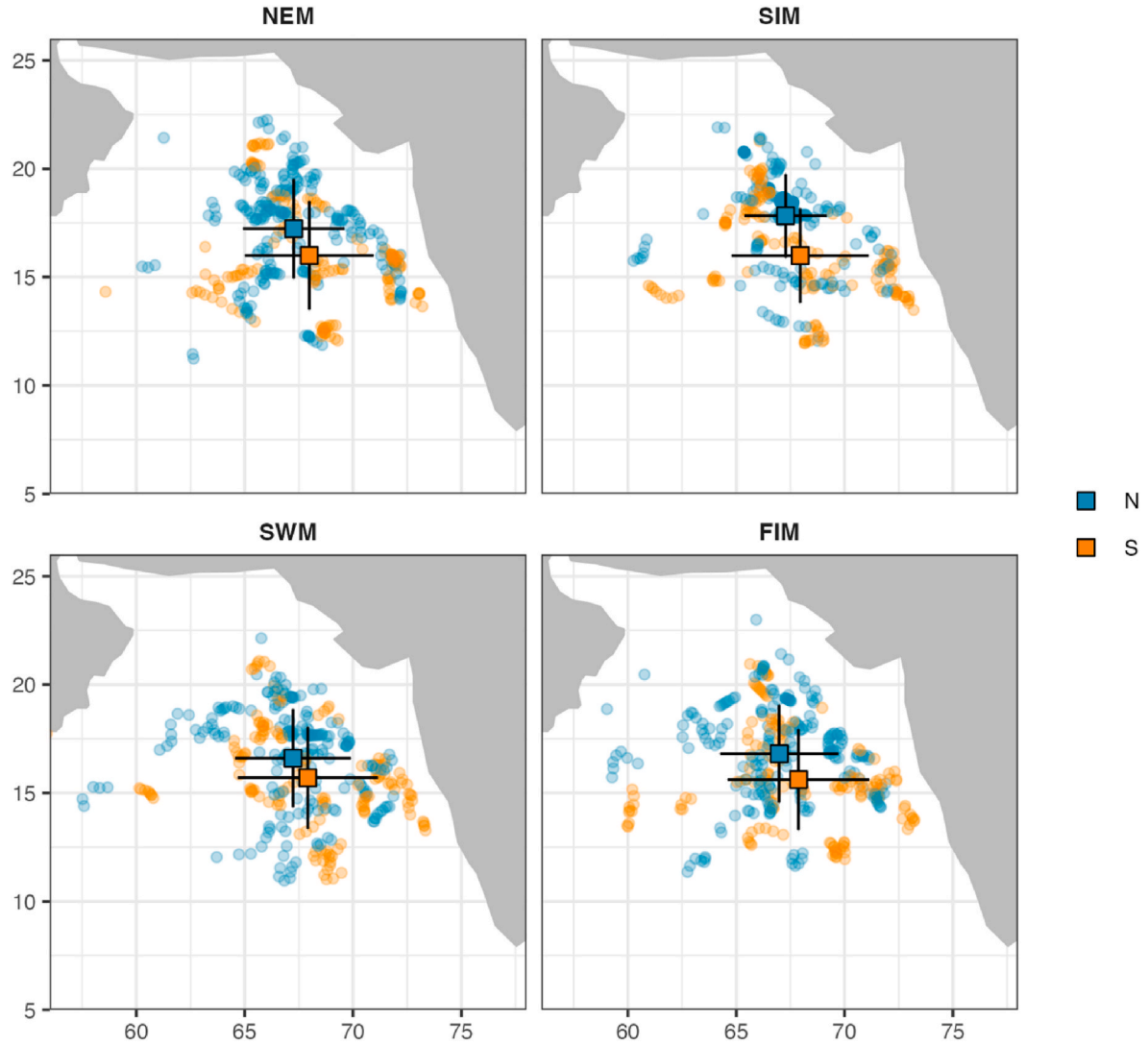

Fig. 1. Distribution of float profiles (deployed between the years 2013 and 2022) included in analyses. Circular markers correspond to BGC-Argo profiles included in analysis, grouped by normal (N, blue) and strong (S, orange) warm pool regimes. Square markers correspond to mean latitude and longitude for each warm pool regime. Whiskers correspond to standard deviation of latitude and longitude for each warm pool regime.

Table 2
Number of BGC-Argo profiles available in each year for BGC-Argo dataset used in this study.

Regime	Year	N	Total
N	2013	87	903
	2014	154	
	2017	161	
	2018	232	
	2021	109	
	2022	160	
S	2015	240	599
	2016	197	
	2019	104	
	2020	58	

performed on interpolated profiles within a moving 3 m window. The thermocline depth was calculated as the depth with the minimum regression slope (representing the depth where temperature decreased the most rapidly).

2.3.3. Determination of average particle size

Average particle area was derived from b_{bp} measurements following the method described by Briggs et al. (2013), using Eq. (1):

$$\overline{A}_{bbp} = \frac{var(b_{bp}\ detrended)}{mean(b_{bp})} \quad \frac{V}{Q_{bbp}} \quad \frac{1}{\alpha(\tau)} \tag{1}$$

As described in Rembauville et al. (2017), b_{bp} detrended was calculated by applying an 11-point rolling median filter to b_{bp} measurements and then subtracting the result from the original b_{bp} profile. Var(b_{bp} detrended) corresponds to the variance of the detrended profile. Mean (b_{bp}) corresponds to the mean value of the original b_{bp} profile. V corresponds to the sample volume (12.5 ml). Q_{bbp} corresponds to backscattering efficiency (0.024). Alpha (0.0967) is a correction to sample volume accounting for the movement of water. Average particle diameter was then calculated as

$$d_{bbp} = 2\sqrt{\overline{A}_{bbp}\pi^{-1}} \tag{2}$$

To calculate average particle diameter within the mixed layer (d_{ML}), d_{bbp} values were then averaged for measurements between 10 m and the mixed layer depth.

2.3.4. Estimation of POC

POC was estimated from b_{bp} (measured at 700 nm) first by estimating b_{bp} at 639 nm following Morel and Maritorena (2001):

$$b_{bp}(639) = b_{bp}(700)\left(\frac{639}{700}\right)^{-1} \tag{3}$$

POC was then calculated following Balch et al. (2001) as

$$POC = *\ 10,641\ *\ b_{bp}(639)^{0.794} \tag{4}$$

2.3.5. Characterization of subsurface light field

Since no floats in the dataset were equipped with PAR sensors to provide the underwater light field, PAR was estimated based on [Chl*a*] following Morel et al. (2007). For each profile, attenuation coefficients for light at 490 nm were calculated from [Chl*a*] measurements using the formula

$$kd_{490} = 0.0166 + a^{*}[Chla]^{b} \tag{5}$$

Following Cornec et al. (2021), coefficients *a* and *b* were defined as 0.0732 and 0.4412, respectively. Attenuation coefficients for PAR were then calculated as

$$kd_{PAR} = 0.0665 + 0.874^{*}kd_{490} - \left(0.00121^{*}kd_{490}{}^{-1}\right) \tag{6}$$

The euphotic zone depth (EZ) was calculated as the depth where kd_{PAR} was first less than or equal to 0.1 (e.g., the depth where surface irradiance was reduced to 0.1% of its surface value). A euphotic zone boundary of 0.1% I_0 was selected to fully capture the range of light levels where photosynthetic growth might be expected to occur (Marra et al., 2014), especially with the formation of deep chlorophyll maxima during the SIM and FIM periods.

2.3.6. b_{bp} profiles and characterization of mesopelagic zone particle stocks

Since b_{bp} profiles are characterized by a distinct and persistent b_{bp} minimum typically coincident with the upper boundary of the OMZ, the mesopelagic zone was defined as the depth range between the b_{bp} minimum and 1000 m. To further characterize variability in particle stocks within this depth range, the mesopelagic zone was divided into four equally-sized segments between the b_{bp} minimum and 1000 m (hereafter $MZ_1 - MZ_4$). The mesopelagic b_{bp} maximum, corresponding to denitrifying bacteria within the OMZ (Rasse et al., 2020), was typically captured within MZ_1. The frequency of large particles within the mesopelagic zone was characterized following Rembauville et al. (2017). Briefly, the number of mesopelagic b_{bp} measurements exceeding 0.001 m^{-1} was summed and normalized to the number of total mesopelagic b_{bp} measurements. Measurements greater than 0.004 m^{-1} were interpreted as being attributable to large motile particles and excluded from analysis.

2.3.7. Determination of net primary production

To integrate differences in [Chl], b_{bp}, and PAR across strong and normal warm pool regimes, we implemented the Carbon Based Productivity Model (CbPM; Westberry et al., 2008) as described in Yang et al. (2021), estimating net primary production as

$$NPP = C_{phyto}\ x\ \mu \tag{7}$$

Where C_{phyto} corresponds to phytoplankton carbon (mg C m^{-3}) and μ corresponds to phytoplankton specific growth rate (d^{-1}). C_{phyto} was calculated based on the empirical relationship presented in Graff et al. (2015):

$$C_{phyto} = 12128\ x\ b_{bp}(470) + 0.59 \tag{8}$$

In calculating C_{phyto}, float measurements of b_{bp} (700) were converted to b_{bp} (470) following Morel and Maritorena (2001):

$$b_{bp}(470) = b_{bp}(700)\left(\frac{470}{700}\right)^{-1} \tag{9}$$

Phytoplankton growth rates were calculated following Westberry et al. (2008) as:

$$\mu = \frac{2^{*}Chl/C_{phyto}{}^{*}(1 - e^{-5I_z})}{0.022 + (0.045 - 0.022)^{*}e^{-3I_z}} \tag{10}$$

Where I_z (mol photon m^{-2} d^{-1}) corresponds to PAR at each depth (z) for a given profile, calculated based on satellite measurements of I_0 and kd_{PAR} estimates from equation (2).

$$I_z = I_0{}^{*}e^{-kd_{PAR}{}^{*}z} \tag{11}$$

Individual [Chl*a*] and b_{bp} profiles used to estimate NPP were smoothed to remove spikes. Following Cornec et al. (2021), a 5-point rolling median filter was applied to [Chl*a*] profiles. For b_{bp} profiles, a 7-point rolling median filter was applied, followed by a 5-point rolling mean filter.

2.4. Statistical methods

All statistical analyses were performed using R 4.0.2 in R Studio (R Core Team, 2024). A summary of the vertical distribution of biogeochemical and bio-optical variables, was obtained by vertically

integrating measurements within MLD, EZ, and MZ_1 – MZ_4 depth horizons. Depth-integrated values for nutrient concentrations and bio-optical parameters were then additionally normalized to the depth of integration. Because most parameters in the dataset had skewed or otherwise non-normal distributions, average values are reported as the median with the bounds of the 95 percent confidence interval for the median, calculated using the MedianCI function in the DescTools package (Signorell et al., 2021). Hypothesis tests were performed using the Wilcoxon Signed Rank Test, unless otherwise indicated. Original least squares regressions were performed for all pairwise comparisons of parameters. Model I linear regressions were performed when comparing random variables to known values (e.g., months, Julian days). Model II linear regressions were performed when comparing pairs of random variables using the lmodel2 package (Legendre, 2018). A significance threshold of p of 0.05 was used for all statistical tests.

3. Results

3.1. Long-term variability in ASMWP strength

Annual average ASMWP index values generally increased from 2002 to 2022, albeit with a large degree of interannual variability (Fig. 2). Notably, WP_{IND} was significantly higher between the years 2013–2022 (T-test; $p = 0.02$) than in earlier years (2003–2012). As noted in the methods section, we focus on differences between normal and strong warm pool years only. We observed six normal warm pool years and four strong warm pool years for the period of study (2013–2022). WP_{IND} values were strongly correlated with average DMI_{FIM} values (Fig. 3A; $R^2 = 0.43$, $p = 0.002$), as well as average SST anomalies within the Western Indian Ocean (e.g., the region within 10°S – 10°N and 50°E – 70°E) during the preceding FIM period (Fig. 3B; $R^2 = 0.74$, $p < 1 \times 10^{-7}$). Within the study area, WP_{IND} values were also strongly correlated with average SST values during the NEM ($R^2 = 0.61$, $p = 4 \times 10^{-5}$), SIM ($R^2 = 0.99$, $p = 4 \times 10^{-52}$) and SWM ($R^2 = 0.30$, $p < 0.01$) periods of the same year.

3.2. Seasonality in AS hydrology and biogeochemistry

Average SST values within the study area were characterized by a bimodal seasonality, with annually maximal SST values occurring during SIM and FIM and annually minimal SST values during NEM and SWM. However, average SST values were significantly higher in strong warm pool years for all months of the year (Fig. 4A). Values for $strI_\sigma$ generally correlated with SST, reaching maximal values during the SIM and FIM periods and minimal values during NEM and SWM. As with SST, $strI_\sigma$ values were significantly higher in strong warm pool years during the NEM and SWM periods (Table 3). Basin-wide wind stress averages reached maximal values during the SWM period (Fig. 4B), with normal warm pool years being characterized by significantly elevated wind stress values during June ($p = 0.0003$) and July ($p = 0.004$). Thermocline depths were characterized by a relatively weak bimodal seasonality, reaching local maxima during the SIM and FIM periods (Fig. 4C). Sea surface height anomalies reached maximal values during the SIM period irrespective of warm pool regime and were significantly elevated in normal warm pool years for all months of the year, both when considering upwelling regions or the central basin alone ($p < 0.0001$ for all comparisons; Fig. 5).

Thermocline depths were significantly greater in normal warm pool years throughout the year, with the exception of the SIM period (Table 3). Seasonality in MLDs was largely similar across warm pool regimes, with no significant differences across warm pool regime for any period of the monsoon cycle (Table 3). Values for $strI_\sigma$ were significantly elevated for strong warm pool years during the NEM and SWM periods, indicating enhanced water column stratification under strong warm pool regimes (Table 3).

3.3. Trends in net primary production and mesopelagic particle stocks

Depth integrated estimates of euphotic zone NPP showed bimodal seasonality, with maximal NPP_{EZ} values occurring in the NEM and SWM periods when algal blooms develop (Table 4, Fig. 6A). However, NPP_{EZ} was significantly lower in strong warm pool years compared to normal warm pool years across all periods of the monsoon cycle (Table 4). NPP_{EZ} was inversely correlated with for $strI_\sigma$ overall (Fig. 7; $r = -0.91$; $p < 0.001$) and during the NEM ($r = -0.97$; $p < 0.001$), SIM ($r = -0.80$; $p = 0.02$), and SWM ($r = -0.81$; $p < 0.001$) periods. NPP_{EZ} was negatively correlated with central basin SSHA during the SIM period ($r = -0.73$, $p = 0.04$). NPP_{EZ} was additionally negatively correlated with SSHA in upwelling regions alone during the SWM period ($r = -0.87$, $p = 0.003$). No significant correlations were observed for comparisons of NPP_{EZ} and MLD.

Particle stocks within the mesopelagic zone showed a unimodal increase over the course of the year, with maximal values typically occurring in August/September, especially in normal warm pool years (Fig. 6A). Although there were no significant differences in particle stocks when averaged across the entire mesopelagic zone, particle stocks were significantly greater within MZ_1 and MZ_2 during SWM and FIM periods in normal warm pool years ($p < 0.001$ for all comparisons). Particle stocks were additionally significantly greater within MZ_3 and MZ_4 during the FIM period in normal warm pool years ($p < 0.02$ for each

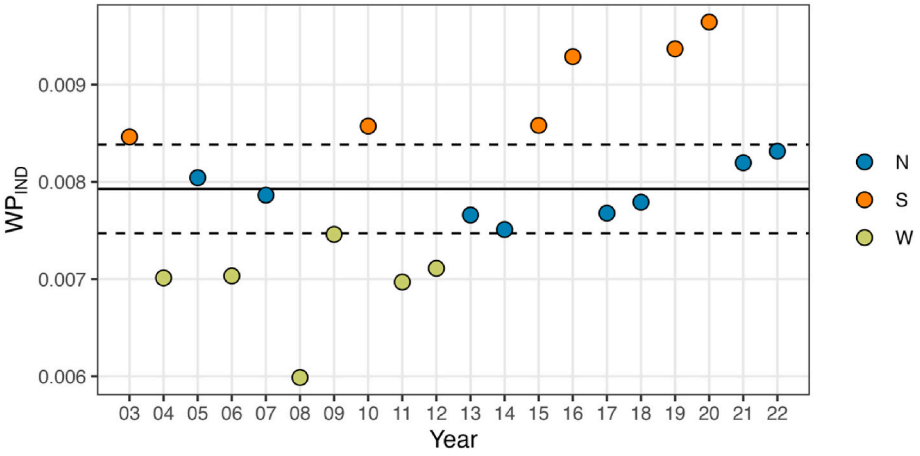

Fig. 2. Average normalized ASMWP index values (WP_{IND}) for 2003–2022. Solid line represents the mean WP_{IND} value for the time series. Dashed line represents the mean $WP_{IND} \pm 0.5$ x the standard deviation of WP_{IND} values for the timeseries. Data grouped by weak warm pool extent (W), normal warm pool extent (N), and strong warm pool extent (S).

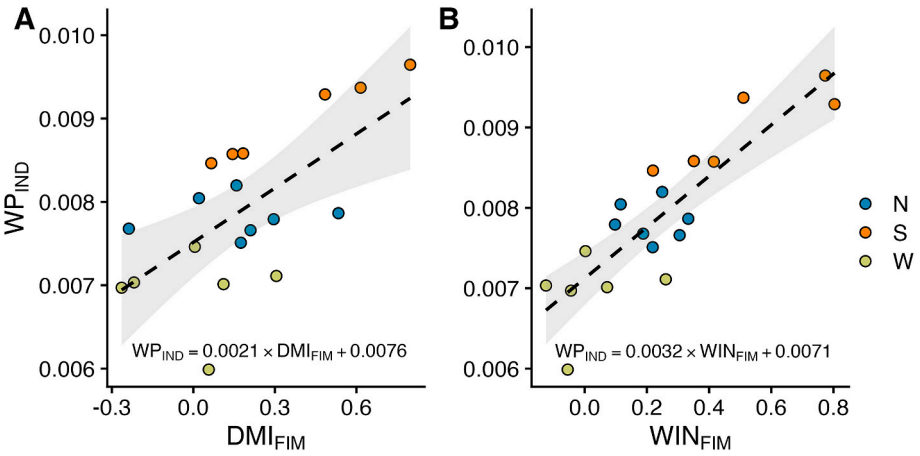

Fig. 3. Comparisons between satellite measured mean warm pool index (WP_{IND}) and **(A)** average Indian Ocean Dipole during the preceding FIM period (DMI_{FIM}); **(B)** average SST anomalies in the Western Indian Ocean during the preceding FIM period (WIN_{FIM}). Data grouped by weak warm pool extent (W), normal warm pool extent (N), and strong warm pool extent (S).

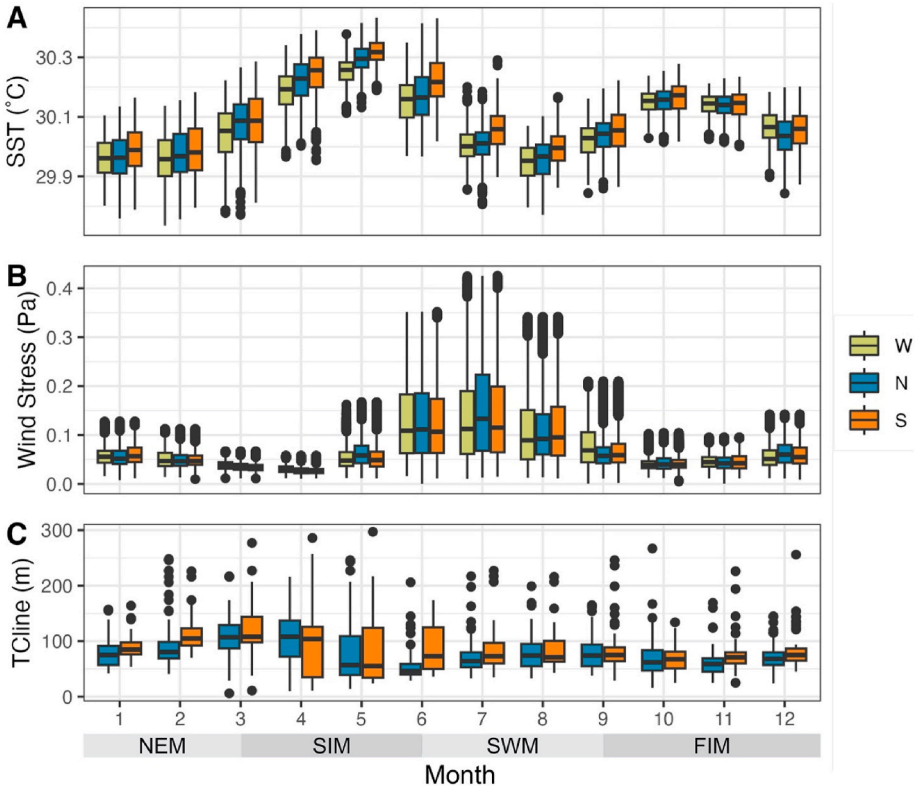

Fig. 4. **(A)** Distribution of satellite measurements of sea surface temperature (SST) within the study region for weak (W), normal (N), and strong (S) warm pool years. **(B)** Basin-wide wind stress magnitude averages over the central Arabian Sea for weak, normal, and strong warm pool years. **(C)** Float-based estimates of thermocline depth for normal and strong warm pool years. X-axis text labels are centered on the median month of the Northeast Monsoon (NEM), Spring Intermonsoon (SIM), Southwest Monsoon (SWM), and Fall Intermonsoon (FIM) periods.

comparison). The relative frequencies of large particles in the mesopelagic zone were significantly greater in normal warm pool years compared to strong warm pool years in the SIM, SWM, and FIM periods (Fig. 8B; $p < 0.03$ for all comparisons). Average particle sizes within the mixed layer were characterized by bimodal seasonality, with average particle sizes reaching maximal values during NEM and SWM periods (Table 4, Fig. 8). However, seasonality in particle sizes were muted during strong warm pool years, with particles being significantly smaller in August compared to normal warm pool years ($p = 0.006$).

4. Discussion

Our results capture a major shift in phytoplankton ecophysiology and carbon export in response to warming ocean temperatures within the Arabian Sea. Strong warm pool years are characterized by a 35 percent reduction in euphotic zone NPP during the highly productive SWM (Fig. 6A), and a 13 percent reduction in particle stocks within the upper mesopelagic zone during the subsequent late SWM/early FIM period (Fig. 6B). Correlations between WP_{IND} and DMI_{FIM} capture a strong connection between ASMWP formation and the strength of the

Table 3
Median values of mixed layer depth (MLD) stratification index ($strI_\sigma$) and Brunt Väisälä frequency at the depth of the MLD (BVF_{MLD}) for normal (N) and strong (S) warm pool years during northeast monsoon (NEM), spring intermonsoon (SIM), southwest monsoon (SWM), and fall intermonsoon (FIM) periods. Upper and lower bounds of 95 percent confidence intervals for each period of the monsoon cycle and regime in parentheses. Asterisks indicate p-values for comparisons of parameter values across warm pool regimes for a given period of the monsoon cycle. *: < 0.05, **: <0.005.

	TCline (m)	MLD (m)	$strI_\sigma$ (kg m^{-3})	BVF_{MLD} x 10^5
NEM (N)	80 (76–85)**	29.5 (26–33)	2.1 (2–2.2)**	1.2 (1–1.4)**
NEM (S)	93.5 (86–97)**	32.5 (26–40)	2.3 (2.2–2.6)**	0.77 (0.7–1)**
SIM (N)	90 (75–100)	19 (17–20)	3.2 (3–3.4)	2.21 (2–2.5)
SIM (S)	100 (85–110)	17 (15–19)	3.4 (3.1–3.6)	2.3 (1.9–2.7)
SWM (N)	65 (62–71)*	42 (39–46)	2.5 (2.5–2.6)*	1.05 (0.9–1.2)
SWM (S)	71 (66–76)*	41 (38–48)	2.7 (2.6–2.8)*	1.03 (0.9–1.1)
FIM (N)	61 (59–65)*	29 (25–32)	2.8 (2.7–2.9)	1.55 (1.2–1.9)
FIM (S)	70 (66–75)*	24 (22–30)	2.9 (2.8–3.1)	1.31 (1.1–1.7)

Indian Ocean Dipole, and suggest that positive IOD events in the fall impact Arabian sea ecology and biogeochemistry not only during the NEM phytoplankton bloom as has previously been reported (Sarma, 2006),

Reduced productivity during the SWM period of strong warm pool years likely results from an intensification of downwelling within the basin, as reflected by increased SSHA (Fig. 5) and deeper thermoclines (Fig. 4). Because mixed layer depths are similar across warm pool regimes, a deepening of the thermocline in strong warm pool years leads to a thickening of the barrier layer (e.g., the layer between the base of the mixed layer and the thermocline), inhibiting the resupply of nutrients to the surface in strong warm pool years despite a similar degree of stratification at the mixed layer boundary compared to normal warm pool years. Indeed, Sarangi and Devi (2017) identified basin-scale inverse relationships between SSHA and nitrate concentrations within the Arabian Sea across 2014 and 2015, which were identified as normal and strong warm pool years in our results, respectively. The thickening of the barrier layer could also inhibit cooling of surface waters (Masson et al., 2005), contributing to enhanced stratification of the water column and associated decreases in primary production (Fig. 7).

Horizontal advection of upwelled nutrients has also previously been identified as a key driver of phytoplankton productivity within the Arabian Sea (Banse, 1987; Prasanna Kumar et al., 2000), and likely contributes to the contrasts in productivity observed in our results. The strong relationships between SSHA within upwelling regions and NPP during the SWM period are especially striking, given the spatial separation of the regions sampled in calculating either parameter and the absence of similar relationships when considering the SSHA measurements from the central basin alone. It is also worth noting that decreases in SWM production during strong warm pool years could additionally be caused by decreases in the availability of regenerated nutrients (Anju et al., 2020) or iron (Naqvi et al., 2010; Guieu et al., 2019).

Observed decreases in average cell size during the peak of the summer monsoon period suggests that this decrease in production may be attributable to a shift toward phytoplankton communities dominated by smaller size classes during strong warm pool years. SWM phytoplankton communities during strong warm pool years may consist primarily of cyanobacteria, as was observed by Goes (unpublished results) during the recently concluded Indo-US EKAMSAT monsoon study cruise of June

Table 4
Median values of bio-optical parameters and modeled net primary production within the study area for normal (N) and strong (S) warm pool regimes for Northeast Monsoon (NEM), Spring Intermonsoon (SIM), Southwest Monsoon (SWM), and Fall Intermonsoon (FIM). Upper and lower bounds of 95 percent confidence intervals for each period of the monsoon cycle and regime in parentheses. Asterisks indicate p-values for comparisons of parameter values across warm pool regimes for a given period of the monsoon cycle. *: <0.05, **: <0.005.

	$[Chla]_{EZ}$ (mg m^{-3})	NPP (mg C m^{-2} d^{-1})	d_{ml} (μm)
NEM (N)	0.22 (0.21–0.23)	1926 (1804–2080)	143 (128–166)
NEM (S)	0.22 (0.21–0.23)	1727 (1435–1924)	168 (128–192)
SIM (N)	0.17 (0.16–0.18)	737 (696–791)	88 (70–109)
SIM (S)	0.17 (0.16–0.18)	632 (574–685)	118 (85–180)
SWM (N)	0.19 (0.18–0.21)	1500 (1384–1713)	196 (154–206)
SWM (S)	0.18 (0.16–0.19)	1005 (917–1212)	148 (134–174)
FIM (N)	0.19 (0.19–0.2)	1262 (1148–1337)	108 (94–125)
FIM (S)	0.19 (0.17–0.2)	1089 (894–1233)	97 (83–115)

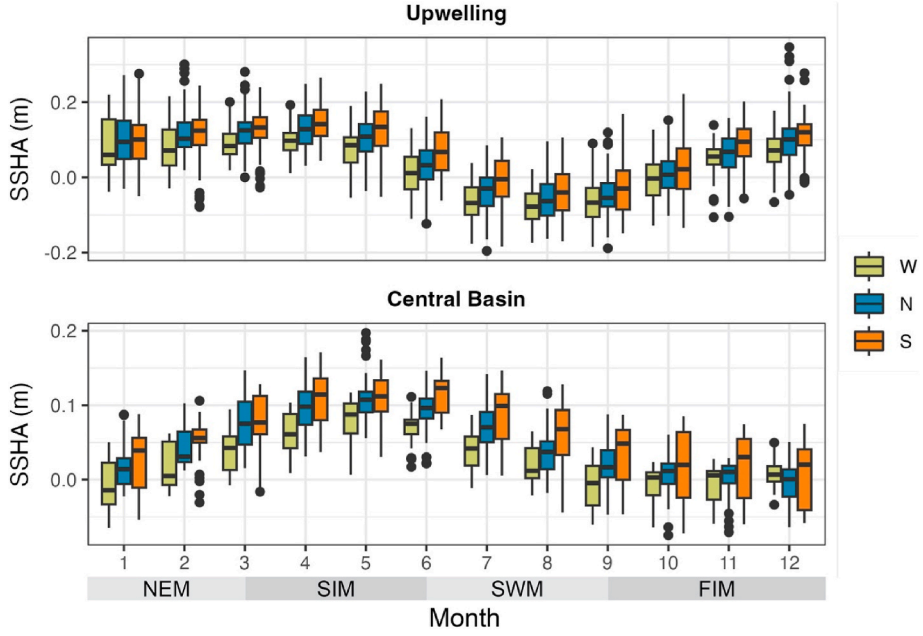

Fig. 5. Distribution of average sea surface height anomalies within central Arabian Sea basin **(Central Basin)** and within upwelling regions alone **(Upwelling)** for weak (W), normal (N), and strong (S) warm pool years. X-axis text labels are centered on the median month of the Northeast Monsoon (NEM), Spring Intermonsoon (SIM), Southwest Monsoon (SWM), and Fall Intermonsoon (FIM) periods.

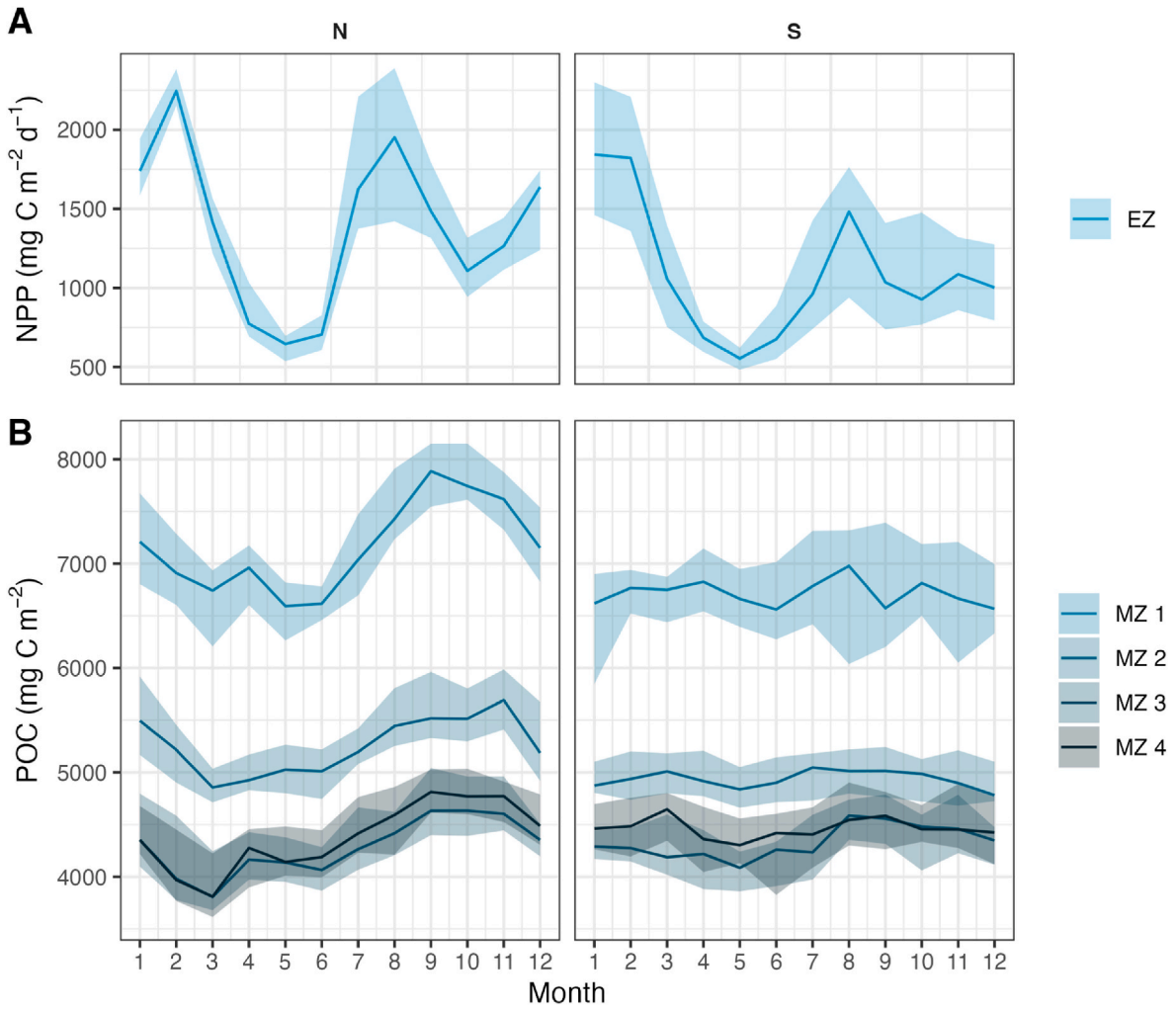

Fig. 6. **(A)** Monthly median depth-integrated NPP values within the euphotic zone (EZ) and **(B)** successive layers of the oxygen minimum zone (MZ_1 – MZ_4) across normal (N) and strong (S) warm pool years. Shading corresponds to bounds of the 95 percent confidence interval of the median.

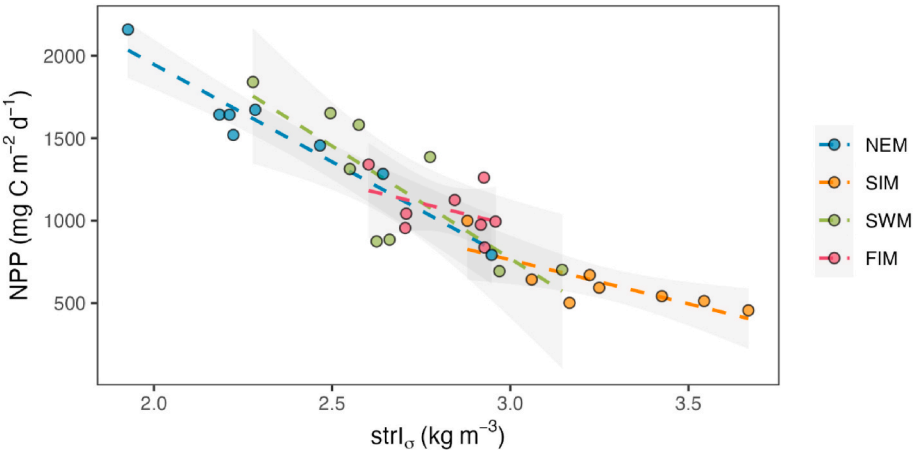

Fig. 7. Comparisons of monthly median stratification index values ($strl_\sigma$) and NPP. Dashed lines correspond to regressions comparing monthly averages for individual periods of the monsoon cycle. Shading corresponds to 95% confidence intervals of regression parameters.

2023, which was during a strong warm pool year. By contrast, during normal years SWM phytoplankton communities may be dominated by larger diatom cells, which require higher nutrient concentrations and are associated with lower sea surface temperatures within the Arabian Sea (Chowdhury et al., 2021). While shifts in community structure have been reported to occur in the Arabian Sea during the NEM period, particularly in response to enhanced stratification and anoxic conditions within the mixed layer (Goes et al., 2020), our results provide evidence of a similar shift during the SWM period.

A shift toward smaller phytoplankton cell size distributions in strong

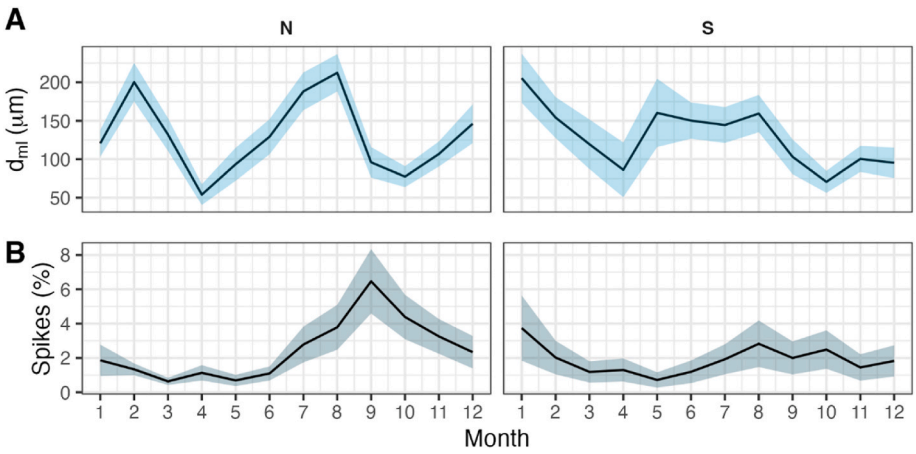

Fig. 8. (A) Monthly median particle diameter within the mixed layer across normal (N) and strong (S) warm pool years. **(B)** Frequency of large particles across normal (N) and strong (S) warm pool years. Shading corresponds to 95 percent confidence interval of the median.

warm pool years may also explain the associated decrease in particle stocks within the upper mesopelagic zone during the late SWM/early FIM period (Fig. 6), in addition to the decrease in the frequency of large particles observed in the mesopelagic zone (Fig. 8B). Late SWM/early FIM export pulses have been well documented in sediment trap studies, and are generally ascribed to the sinking of particles generated during the SWM phytoplankton bloom (Nair et al., 1989; Buesseler et al., 1998), in particular diatoms (Barlow et al., 1999; Garrison et al., 2000; Chowdhury et al., 2021). Garrison et al. (2000) specifically identified correlations between diatom abundance and carbon fluxes during the SWM period, while Haake et al. (1993) reported the export of biogenic opal to peak in September, consistent with the peak in MZ_1 POC observed in our results.

Time series of particle stocks within the mesopelagic zone (Fig. 6) additionally highlight seasonal and interannual variability in relationships between euphotic zone production and mesopelagic particle stocks. While previous studies have reported only weak correlations between particle stocks across the euphotic and mesopelagic zones (Wojtasiewicz et al., 2020; Bock et al., 2022), our results suggest particles exported from the euphotic zone account for a significant fraction of the overall b_{bp} signal in normal warm pool years, in particular during the SWM period. However, this relationship could be obscured if the interannual variability in warm pool extent or the approximate 1-month time lag between the periods of maximal particle stocks in the euphotic zone (July–August) and in the upper mesopelagic zone (August–September) is not taken into account.

5. Conclusion

These results suggest that the extent of the ASMWP exerts a strong influence on primary production and particle export within the Central Arabian Sea. Specifically, increased warm pool magnitude appears to be associated with the intensification of downwelling and a subsequent deepening of the thermocline during the SWM period, inhibiting the supply of nutrients to the euphotic zone, potentially in response to positive IOD events during the preceding fall. Decreases in primary production during the SWM period specifically appear to be associated with a shift toward phytoplankton communities dominated by small cells, leading to a corresponding decrease in particle export to the mesopelagic zone during the late SWM/early FIM period.

It is especially remarkable that these changes were associated with relatively small differences in SST within the Arabian Sea. Indeed, the observed 35 percent decrease in primary production during the SWM period in strong warm pool years was associated with an average increase in SST of only 0.05 °C during the preceding SIM period. Given the estimated warming rate of 0.1 °C/decade within the AS (Roxy et al., 2016) and the increased frequency of positive IOD years over the last 60 years (Cai et al., 2009), further temperature increases could have dramatic impacts on production and export within the basin, with implications for overall ecosystem health, the food web and functioning of the biological carbon pump.

CRediT authorship contribution statement

Nicholas Bock: Conceptualization, Data curation, Formal analysis, Investigation, Methodology, Project administration, Resources, Software, Visualization, Writing – original draft, Writing – review & editing. **Joaquim Goes:** Conceptualization, Funding acquisition, Investigation, Methodology, Supervision, Validation, Writing – review & editing. **Hervé Claustre:** Formal analysis, Methodology, Supervision, Writing – review & editing. **Vincent Taillandier:** Formal analysis, Writing – review & editing. **Helga do Rosario Gomes:** Conceptualization, Investigation, Methodology, Project administration, Supervision, Writing – review & editing.

Funding sources

This work was funded by a European Union Marie Sklodowska-Curie Postdoctoral Fellowship (grant number 101064055). Views and opinions expressed are however those of the author(s) only and do not necessarily reflect those of the European Union or Horizon Europe. Neither the European Union nor the granting authority can be held responsible for them. JIG and HRG are supported by grants from NASA (#80NSSC20K0014 and 80NSSC24K0893), NSF (#2019983), and NOAA-GST SA18-CUNY01.

Declaration of competing interest

The authors declare that they have no known competing financial interests or personal relationships that could have appeared to influence the work reported in this paper.

Acknowledgments

The authors thank Nathan Briggs for communication and feedback concerning the appropriate implementation of methods for characterizing particle diameter and spike frequency. Float data used in this study were collected and made freely available by the International Argo Program and the national programs that contribute to it. (https://argo.ucsd.edu, https://www.ocean-ops.org). The Argo Program is part of the Global Ocean Observing System.

Appendix A. Supplementary data

Supplementary data to this article can be found online at https://doi.org/10.1016/j.dsr.2024.104406.

Data availability

Data will be made available on request.

References

Anju, M., Sreeush, M.G., Valsala, V., Smitha, B.R., Hamza, F., Bharathi, G., et al., 2020. Understanding the role of nutrient limitation on plankton biomass over Arabian Sea via 1-D coupled biogeochemical Model and bio-argo observations. J. Geophys. Res. Ocean. 125, 1–28. https://doi.org/10.1029/2019JC015502.

Argo, 2024. Argo Float Data and Metadata from Global Data Assembly Centre (Argo GDAC). SEANOE. https://doi.org/10.17882/42182.

Balch, W.M., Drapeau, D.T., Fritz, J.J., Bowler, B.C., Nolan, J., 2001. Optical backscattering in the Arabian Sea - continuous underway measurements of particulate inorganic and organic carbon. Deep. Res. Part I Oceanogr. Res. Pap. 48, 2423–2452. https://doi.org/10.1016/S0967-0637(01)00025-5.

Banse, K., 1987. Seasonality of phytoplankton chlorophyll in the central and northern Arabian sea. Deep-Sea Res., Part A 34, 713–723. https://doi.org/10.1016/0198-0149(87)90032-X.

Banse, K., McClain, C., 1986. Winter blooms of phytoplankton in the Arabian Sea as observed by the coastal zone color scanner. Mar. Ecol. Prog. Ser. 34, 201–211. https://doi.org/10.3354/meps034201.

Barlow, R.G., Mantoura, R.F.C., Cummings, D.G., 1999. Monsoonal influence on the distribution of phytoplankton pigments in the Arabian Sea. Deep. Res. Part II Top. Stud. Oceanogr. 46, 677–699. https://doi.org/10.1016/S0967-0645(98)00123-4.

Bauer, S., Hitchcock, G.L., Olson, D.B., 1991. Influence of monsoonally-forced Ekman dynamics upon surface layer depth and plankton biomass distribution in the Arabian Sea. Deep-Sea Res., Part A 38, 531–553. https://doi.org/10.1016/0198-0149(91)90062-K.

Behrenfeld, M.J., O'Malley, R.T., Siegel, D.A., McClain, C.R., Sarmiento, J.L., Feldman, G.C., et al., 2006. Climate-driven trends in contemporary ocean productivity. Nature 444, 752–755. https://doi.org/10.1038/nature05317.

Bock, N., Cornec, M., Claustre, H., Duhamel, S., 2022. Biogeographical classification of the Global Ocean from BGC-argo floats. Global Biogeochem. Cycles 36, 1–24. https://doi.org/10.1029/2021gb007233.

Briggs, N.T., Slade, W.H., Boss, E., Perry, M.J., 2013. Method for estimating mean particle size from high-frequency fluctuations in beam attenuation or scattering measurements. Appl. Opt. 52, 6710–6725. https://doi.org/10.1364/AO.52.006710.

Buesseler, K., Ball, L., Andrews, J., Benitez-Nelson, C., Belastock, R., Chai, F., et al., 1998. Upper ocean export of particulate organic carbon in the Arabian Sea derived from thorium-234. Deep. Res. Part II Top. Stud. Oceanogr. 45, 2461–2487. https://doi.org/10.1016/S0967-0645(98)80022-2.

Cai, W., Sullivan, A., Cowan, T., 2009. Climate change contributes to more frequent consecutive positive Indian Ocean Dipole events. Geophys. Res. Lett. 36, 1–5. https://doi.org/10.1029/2009GL040163.

Chowdhury, M., Biswas, H., Mitra, A., Silori, S., Sharma, D., Bandyopadhyay, D., et al., 2021. Southwest monsoon-driven changes in the phytoplankton community structure in the central Arabian Sea (2017–2018): after two decades of JGOFS. Prog. Oceanogr. 197, 102654. https://doi.org/10.1016/j.pocean.2021.102654.

Cornec, M., Claustre, H., Mignot, A., Guidi, L., Lacour, L., Poteau, A., et al., 2021. Deep chlorophyll maxima in the Global Ocean: occurrences, drivers and characteristics. Global Biogeochem. Cycles 35, 1–30. https://doi.org/10.1029/2020gb006759.

Currie, R.I., Fisher, A.E., Hargreaves, P.M., 1973. Arabian Sea upwelling. In: Zeitzshel, B. (Ed.), The Biology of the Indian Ocean. Springer, New York, pp. 37–52.

Deepa, R., Gnanaseelan, C., Deshpande, M., Salvekar, P.S., 2012. A Model study on understanding the influence of Arabian Sea mini warm pool on monsoon onset vortex formation. Pure Appl. Geophys. 169, 1693–1706. https://doi.org/10.1007/s00024-011-0406-z.

Fournier, S., Willis, J., Killett, E., Qu, Z., Zlotnicki, V., 2022. JPL MEaSUREs gridded Sea Surface height anomalies version 2205. https://doi.org/10.5067/SLREF-CDRV3.

Garrison, D.L., Gowing, M.M., Hughes, M.P., Campbell, L., Caron, D.A., Dennett, M.R., et al., 2000. Microbial food web structure in the Arabian Sea: a US JGOFS study. Deep. Res. Part II Top. Stud. Oceanogr. 47, 1387–1422. https://doi.org/10.1016/S0967-0645(99)00148-4.

Goes, J.I., Thoppil, P.G., Gomes, H. do R., Fasullo, J.T., 2005. Warming of the eurasian landmass is making the Arabian Sea more productive. Science 308, 545–547. https://doi.org/10.1126/science.1106610.

Goes, J.I., Tian, H., Gomes, H. do R., Anderson, O.R., Al-Hashmi, K., deRada, S., et al., 2020. Ecosystem state change in the Arabian Sea fuelled by the recent loss of snow over the Himalayan-Tibetan Plateau region. Sci. Rep. 10, 2–9. https://doi.org/10.1038/s41598-020-64360-2.

Graff, J.R., Westberry, T.K., Milligan, A.J., Brown, M.B., Dall'Olmo, G., van Dongen-Vogels, V., et al., 2015. Analytical phytoplankton carbon measurements spanning diverse ecosystems. Deep. Res. Part I Oceanogr. Res. Pap. 102, 16–25. https://doi.org/10.1016/j.dsr.2015.04.006.

Guieu, C., Al Azhar, M., Aumont, O., Mahowald, N., Levy, M., Ethé, C., et al., 2019. Major impact of dust deposition on the productivity of the Arabian Sea. Geophys. Res. Lett. 46, 6736–6744. https://doi.org/10.1029/2019GL082770.

Haake, B., Ittekkot, V., Rixen, T., Ramaswamy, V., Nair, R.R., Curry, W.B., 1993. Seasonality and interannual variability of particle fluxes to the deep Arabian sea. Deep. Res. Part I 40, 1323–1344. https://doi.org/10.1016/0967-0637(93)90114-I.

Honjo, S., Manganini, S.J., Krishfield, R.A., Francois, R., 2008. Particulate organic carbon fluxes to the ocean interior and factors controlling the biological pump: a synthesis of global sediment trap programs since 1983. Prog. Oceanogr. 76, 217–285. https://doi.org/10.1016/j.pocean.2007.11.003.

Legendre, P., 2018. lmodel2: Model II regression. Available at: https://cran.r-project.org/package=lmodel2.

Marra, J.F., Lance, V.P., Vaillancourt, R.D., Hargreaves, B.R., 2014. Resolving the ocean's euphotic zone. Deep. Res. Part I Oceanogr. Res. Pap. 83, 45–50. https://doi.org/10.1016/j.dsr.2013.09.005.

Masson, S., Luo, J.J., Madec, G., Vialard, J., Durand, F., Gualdi, S., et al., 2005. Impact of barrier layer on winter-spring variability of the southeastern Arabian Sea. Geophys. Res. Lett. 32, 1–4. https://doi.org/10.1029/2004GL021980.

Morel, A., Maritorena, S., 2001. Bio-optical properties of oceanic waters: a reappraisal. J. Geophys. Res. Ocean. 106, 7163–7180. https://doi.org/10.1029/2000jc000319.

Morel, A., Gentili, B., Claustre, H., Babin, M., Bricaud, A., Ras, J., et al., 2007. Optical properties of the "clearest" natural waters. Limnol. Oceanogr. 52, 217–229. https://doi.org/10.4319/lo.2007.52.1.0217.

Nair, R.R., Ittekkot, V., Manganini, S.J., Ramaswamy, V., Haake, B., Degens, E.T., et al., 1989. Increased particle flux to the deep ocean related to monsoons. Nature 338, 749–751. https://doi.org/10.1038/338749a0.

Naqvi, S.W.A., Moffett, J.W., Gauns, M.U., Narvekar, P.V., Pratihary, A.K., Naik, H., et al., 2010. The Arabian Sea as a high-nutrient, low-chlorophyll region during the late Southwest Monsoon. Biogeosciences 7, 2091–2100. https://doi.org/10.5194/bg-7-2091-2010.

NASA Ocean Biology Processing Group, 2022. Suomi-NPP VIIRS Level 3 Mapped Photosynthetically Available Radiation Data, Version R2022.0.

NASA/JPL, 2022. GHRSST Level 4 MUR Global Foundation Sea Surface Temperature Analysis (v4.1).

Neema, C.P., Hareeshkumar, P.V., Babu, C.A., 2012. Characteristics of Arabian Sea mini warm pool and Indian summer monsoon. Clim. Dynam. 38, 2073–2087. https://doi.org/10.1007/s00382-011-1166-2.

NOAA, 2024. Wind Stress, Metop-A ASCAT, 0.25°, Global, Near Real Time, 2009-present (Monthly).

Prasanna Kumar, S., Madhupratap, M., Dileep Kumar, M., Gauns, M., Muraleedharan, P. M., Sarma, V.V.S.S., et al., 2000. Physical control of primary productivity on a seasonal scale in central and eastern Arabian Sea. Proc. Indian Acad. Sci. Earth Planet Sci. 109, 433–441. https://doi.org/10.1007/bf02708331.

R Core Team, 2024. A Language and Environment for Statistical Computing. R Foundation for Statistical Computing, Vienna. Austria. http://www.R-project.org.

Ramaswamy, V., Nair, R.R., 1994. Fluxes of material in the Arabian Sea and Bay of bengal - sediment trap studies. Proc. Indian Acad. Sci. Earth Planet Sci. 103, 189–210. https://doi.org/10.1007/BF02839536.

Rao, R.R., Sivakumar, R., 1999. On the possible mechanisms of the evolution of a mini-warm pool during the pre-summer monsoon season and the genesis of onset vortex in the south-eastern Arabian Sea. Q. J. R. Meteorol. Soc. 125, 787–809. https://doi.org/10.1256/smsqj.55502.

Rao, R.R., Jitendra, V., GirishKumar, M.S., Ravichandran, M., Ramakrishna, S.S.V.S., 2015. Interannual variability of the Arabian Sea warm pool: observations and governing mechanisms. Clim. Dynam. 44, 2119–2136. https://doi.org/10.1007/s00382-014-2243-0.

Rasse, R., Claustre, H., Poteau, A., 2020. The suspended small-particle layer in the oxygen-poor Black Sea: a proxy for delineating the effective N2-yielding section. Biogeosciences 17, 6491–6505. https://doi.org/10.5194/bg-17-6491-2020.

Rembauville, M., Briggs, N., Ardyna, M., Uitz, J., Catala, P., Penkerc'h, C., et al., 2017. Plankton assemblage estimated with BGC-argo floats in the southern ocean: implications for seasonal successions and particle export. J. Geophys. Res. Ocean. 122, 8278–8292. https://doi.org/10.1002/2017JC013067.

Rixen, T., Cowie, G., Gaye, B., Goes, J., Do Rosário Gomes, H., Hood, R.R., et al., 2020. Reviews and syntheses: present, past, and future of the oxygen minimum zone in the northern Indian Ocean. Biogeosciences 17, 6051–6080. https://doi.org/10.5194/bg-17-6051-2020.

Roxy, M.K., Modi, A., Murtugudde, R., Valsala, V., Panickal, S., Prasanna Kumar, S., et al., 2016. A reduction in marine primary productivity driven by rapid warming over the tropical Indian Ocean. Geophys. Res. Lett. 43, 826–833. https://doi.org/10.1002/2015GL066979.

Sarangi, R.K., Devi, K.N., 2017. Space-based observation of chlorophyll, sea surface temperature, nitrate, and sea surface height anomaly over the Bay of Bengal and Arabian Sea. Adv. Space Res. 59, 33–44. https://doi.org/10.1016/j.asr.2016.08.038.

Sarma, V.V.S.S., 2006. The influence of Indian Ocean Dipole (IOD) on biogeochemistry of carbon in the Arabian Sea during 1997-1998. J. Earth Syst. Sci. 115, 433–450. https://doi.org/10.1007/BF02702872.

Schmechtig, C., Poteau, A., Claustre, H., D'Ortenzio, F., Boss, E., 2015. Processing bio-argo chlorophyll-a concentration at the DAC level. Argo Data Manag. 1–22.

Schmechtig, C., Poteau, A., Claustre, H., D'Ortenzio, F., Dall'Olmo, G., Boss, E.S., 2018a. Bio-Argo quality control manual for Chlorophyll-A concentration, 1–16. https://doi.org/10.13155/39459.

Schmechtig, C., Poteau, A., Claustre, H., D'Ortenzio, F., Dall'Olmo, G., Boss, E.S., 2018b. Processing BGC-Argo particle backscattering at the DAC level, 1–15. https://doi.org/10.13155/39459.

Signorell, A., 2021. DescTools: Tools for Descriptive Statistics.

Thierry, V., Gilbert, D., Kobayashi, T., 2011. Processing Argo OXYGEN data at the DAC level. AST-10 Meet 1–12.

Thierry, V., Bittig, H., Team, A.-B., 2021. Argo quality control manual for dissolved oxygen concentration. Argo Data Manag. 1–33, v2.1.

Westberry, T., Behrenfeld, M.J., Siegel, D.A., Boss, E., 2008. Carbon-based primary productivity modeling with vertically resolved photoacclimation, 22, 1–18. https://doi.org/10.1029/2007GB003078.

Wojtasiewicz, B., Trull, T.W., Udaya Bhaskar, T.V.S., Gauns, M., Prakash, S., Ravichandran, M., et al., 2020. Autonomous profiling float observations reveal the dynamics of deep biomass distributions in the denitrifying oxygen minimum zone of the Arabian Sea. J. Mar. Syst. 207, 103103. https://doi.org/10.1016/j.jmarsys.2018.07.002.

Wong, A., Keeley, R., Carval, T., et al., 2020. Argo quality control manual for CTD and trajectory data. https://doi.org/10.13155/33951.

Xing, X., Claustre, H., Blain, S., D'Ortenzio, F., Antoine, D., Ras, J., et al., 2012. Quenching correction for in vivo chlorophyll fluorescence acquired by autonomous platforms: a case study with instrumented elephant seals in the Kerguelen region (Southern Ocean). Limnol Oceanogr. Methods 10, 483–495. https://doi.org/10.4319/lom.2012.10.483.

Yang, B., Fox, J., Behrenfeld, M.J., Boss, E.S., Haëntjens, N., Halsey, K.H., et al., 2021. In situ estimates of net primary production in the western north atlantic with Argo profiling floats. J. Geophys. Res. Biogeosciences. 126, 1–16. https://doi.org/10.1029/2020JG006116.